Design of a Resonant-Cavity-Enhanced Photodetector for High-Speed Applications

Hsin-Han Tung and Chien-Ping Lee, *Senior Member, IEEE*

***Abstract*—We present a theoretical study of the effects of light field distribution on the frequency response of a resonant-cavity-enhanced p-i-n photodetector. Taking advantage of the flexibility of cavity design, one can tailor the light field distribution in the absorption region. Because of the difference in velocities of the carriers, the speed performances of the detector depend on the field distribution and the cavity design. The results of our work indicate that when the maximum of light field intensity happens near the p^+ edge of the depletion layer, the device shows the best speed performance. The frequency response, the impulse response, and the step response have been calculated for different structures to demonstrate the importance of the field distribution.**

***Index Terms*—Frequency response, impulse response, quantum efficiency, resonant-cavity-enhanced photodector, step response.**

I. Introduction

HIGH-SPEED and high-sensitivity photodetectors are important for high-bit-rate optical communication systems [1], [2]. The detectors are required to have a wide bandwidth and a high quantum efficiency. For conventional p-i-n photodiodes, the quantum efficiency η is limited by the absorption coefficient α and the absorbing layer thickness d. The highest η obtainable for detectors with a perfect antireflecting coating is $\eta = 1 - \exp(-\alpha d)$. To achieve high η, a thick absorbing layer is required. However, a thick absorbing layer means a long carrier transit time which reduces the device's speed. Resonant-cavity-enhanced (RCE) photodetectors provide a solution to this problem [3], [4]. For such detectors, a thin absorbing layer is put inside a Fabry–Perot cavity. The feedback mirrors of the Fabry–Perot cavity are usually comprised of quarter wavelength stacks (QWS's) [5] with a periodic modulation of the refractive index. At resonance, construction interference is built up within the cavity to enhance the internal optical field intensity. Since the generation rate, g, of the electron-hole pairs is proportional to the light intensity J_{ph}, i.e., $g = \alpha J_{ph}, g$ can be greatly enhanced. So only a very thin absorbing layer is needed to achieve high quantum efficiency. RCE photodetectors with nearly 100% quantum efficiency [6], [7] have been demonstrated.

Manuscript received July 8, 1996; revised January 22, 1997. This work was supported by the National Science Council of the Republic of China under Contract NSC84-2215-E009-039.

H.-H. Tung is with the Department of Electrical Engineering, National Lien-Ho Junior College of Technology and Commerce, Miao Li, Taiwan, R.O.C.

C.-P. Lee is with the Department of Electronics Engineering, National Chiao Tung University, Hsin Chu, Taiwan, R.O.C.

Publisher Item Identifier S 0018-9197(97)03065-0.

The speed of a photodetector is primarily determined by the combined effect of the capacitance of the detector and the transit time for the photocarriers to move through the absorbing layer. For a high-speed detector, the transit time has to be very short. When the area of the detectors is made sufficiently small, the influence from the capacitance is reduced and the effect of the transit time dominates. Wey *et al*. have demonstrated a 2 μm$\times$ 2 μm GaInAs–InP p-i-n photodiode with a 3-dB bandwidth as high as 110 GHz [8], [9]. Bowers and Burrus have indicated that bandwidths in excess of 200 GHz should be possible [10].

For high-speed operation, the electric field throughout the intrinsic layer should be very high so that the carriers travel at the saturation velocity during most of the transit. Usually the electron saturation velocity is greater than the hole saturation velocity; taking advantage of this property, one can improve speed performance for proper device designs. On the other hand, the distributions of photogenerated carriers can also have significant influence on the speed response because the average distance that carriers travel depends on the distribution. In this paper, the performances of RCE photodetectors with different carrier profiles as a result of different cavity design are compared. We found that by proper design, we can tailor the carrier profile in the absorbing region to maximize the speed of the detector.

II. RCE p-i-n Photodiode

Fig. 1 shows the schematic diagram of a RCE p-i-n photodiode used in this study. The structure is similar to that designed by Tang *et al*. [7]. The thickness of the p^+, i, n^+ layers are denoted as L_p, L_i, and L_n, respectively. The front mirror is composed of a half-λ-thick SiO_2 plus one Si-SiO_2 quarter-wave pair, and the back mirror consists of a 0.5λ-thick GaAs layer and a 27-period GaAs-AlAS QWS, where λ is the designed wavelength, 1.3 μm, divided by the refractive index of the material. The absorption coefficient of the intrinsic InGaAs layer is assumed to be $1.16 \times 10^4\,\mathrm{cm}^{-1}$ at 1.3 μm. The quantum efficiency of the resonant detector can be calculated numerically by using the transfer-matrix method (TMM) [11] and is equal to $1-R-T$, where R is the power reflectivity and T is the power transmission. Fig. 2 shows the calculated quantum efficiency versus wavelength for $L_p = 3/4\,\mu$m, $L_i = 1/4\,\mu$m, and $L_n = 5/4\,\mu$m. The dashed curve is for the reference photodiode without a resonant cavity. It is noticed that the quantum efficiency is significantly increased by a factor of 10 (from 10% to nearly 100%) at 1.3 μm.

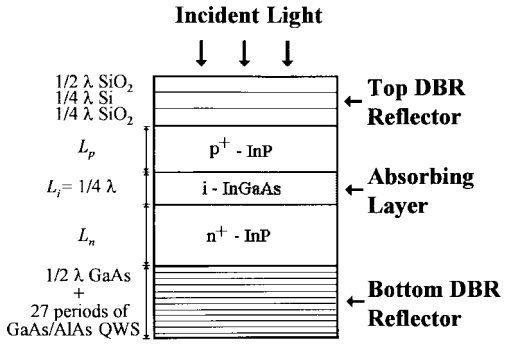

Fig. 1. Schematic representation of the studied RCE p-i-n photodetector. Here λ is the design wavelength, 1.3 μm, divided by the refractive index of each layer.

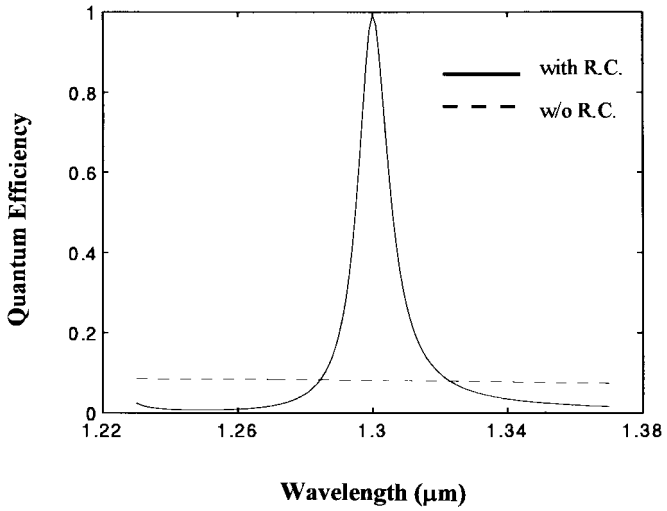

Fig. 2. Calculated quantum efficiency for the studied RCE photodiode with $L_p = 3/4\lambda, L_i = 1/4\lambda$, and $L_n = 5/4\lambda$ (solid line). The diode is designed at 1.3-μm wavelength. Quantum efficiency for conventional photodiode without resonant cavity is also shown for comparison (dashed line).

The quantum efficiency of the resonant detector can be also obtained approximately as [12] (1), shown at the bottom of the page, where R_1 and R_2 are reflectivities of the top and bottom mirrors, respectively, θ_k is the round-trip phase delay of the resonant mode within the cavity, and k is the resonant mode. The effective absorption coefficient, $\alpha_{\text{eff}} = \alpha S$, and the factor S is between 0 and 2 depending on the standing wave effect. From [12], we know that when the condition

$$R_1 = R_2 \exp(-2\alpha_{\text{eff}} L_i) \tag{2}$$

is satisfied, the quantum efficiency at a certain $\alpha_{\text{eff}} L_i$ value is maximized. The parameters we use in the present calculation at $\lambda = 1.3\,\mu$m yield $\theta_k \cong 2k\pi(k = 4), S \cong 1, R_1 \cong 0.8, R_2 \cong 1$ and $\alpha_{\text{eff}} L_i \cong 0.1077$. Under such conditions, (2) is approximately satisfied. Substituting these values into (1), we get $\eta \cong 100\%$. This means the studied RCE photodiode structure has been optimized and the resonant wavelength is 1.3 μm.

To obtain high quantum efficiency, RCE photodetectors have to be operated at the resonant condition. But even at resonance, one still has the flexibility to change the thickness of individual layers as long as the round trip phase delay is $2k\pi$. As will be described later, one can vary and therefore optimize the device's speed performance while keeping the devices at resonance with high quantum efficiencies by adjusting the thickness of certain layers. If we vary the ratio Lp/Ln but keep $L_p + L_n = 2\lambda$ and all other structure parameters the same, we can obtain the quantum efficiencies for devices with various combinations of L_p and L_n at the resonant condition. Fig. 3 shows the quantum efficiency for the RCE photodiode versus the ratio L_p/L_n calculated by the TMM method. It can be seen that η is nearly 100% at $L_p(L_n) = 3/2((1/2\lambda), 5/4\lambda(3/4\lambda), \lambda(\lambda), 3/4\lambda(5/4\lambda)$, and $1/2\lambda(3/2\lambda)$. The quantum efficiency changes periodically whenever L_p (or L_n) changes by $1/2\lambda$. Because of the nature of this periodic property, there are only two distinct L_p/L_n ratios (namely, $L_p(L_n) = \lambda(\lambda)$ and $3/4\lambda(5/4\lambda)$), which have (nearly) 100% quantum efficiency but different field distributions in the cavity. Fig. 4 shows the light field intensity as a function of position of these two combinations. For $L_p = \lambda, L_n = \lambda$, we find the maximum of light intensity occurs near the p^+ edge of the i region, and the result is shown in Fig. 4(a). On the contrary, for $L_p = 3/4\lambda, L_n = 5/4\lambda$, the maximum of the field intensity occurs near the n^+ edge of the i region [see Fig. 4(b)]. The two different and nonuniform light intensity distributions have different influence on the speed response of this diode and will be discussed in next section. Also shown in Fig. 4 is the light intensity of a conventional p-i-n photodiode for comparison (dashed line); a significant increase in the light intensity can be clearly seen.

III. Frequency Response of RCE Photodiode

From Figs. 3 and 4, we know that at the resonant condition when $L_p + L_n = 2\lambda$ there are two different light field distributions for two different L_p/L_n ratios. Since the carrier generation rate is proportional to the light intensity, we can thereby obtain different distributions of photogenerated carriers within the i layer. For convenience, we call the light field profile in Fig. 4(a) "Profile 1" and the light field profile in Fig. 4(b) "Profile 2." Fig. 5 shows the photocarrier distributions for these two different light field profiles. In Fig. 5(a), most of the carriers are generated near the p^+ edge of the i layer, while in Fig. 5(b) most of the carriers are generated near the n^+ edge of the i layer. Taking into account the difference in the drift velocities of the carriers and the nonuniform distribution of the generated carriers in the i region, we calculate the frequency response of the diode below.

$$\eta = \left[\frac{1 + R_2 \exp(-\alpha_{\text{eff}} L_i)}{1 - 2\sqrt{R_1 R_2}\exp(-\alpha_{\text{eff}} L_i)\cos(\theta_k) + R_1 R_2 \exp(-2\alpha_{\text{eff}} L_i)}\right](1 - R_1)(1 - \exp(\alpha_{\text{eff}} L_i)) \tag{1}$$

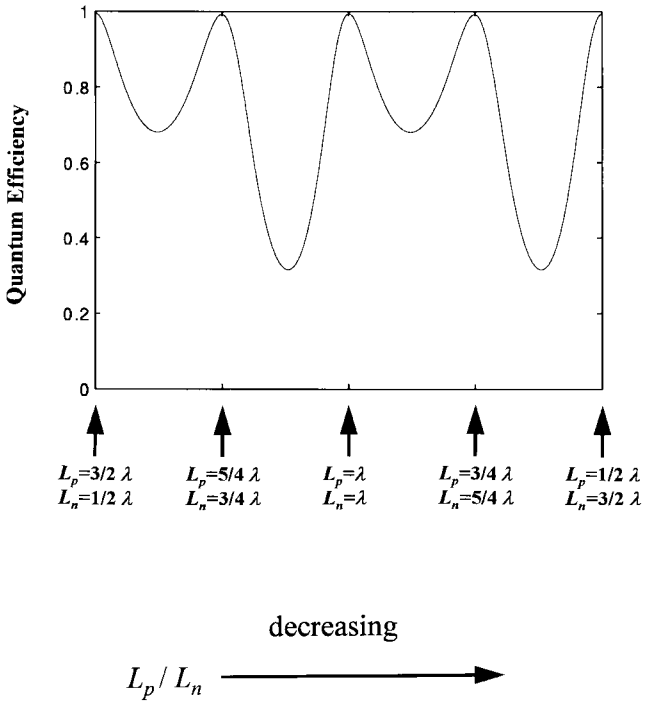

Fig. 3. Thickness dependence of the quantum efficiency for various combinations of L_p and L_n. To operate the RCE photodiode at the resonant condition, $L_p + L_n$ is kept as a constant of 2λ.

We start with the linearized continuity equations for the electrons and holes [13]

$$\frac{\partial p(x,t)}{\partial t} + v_p \frac{\partial p(x,t)}{\partial x} = g(x,t)$$
$$\frac{\partial n(x,t)}{\partial t} - v_n \frac{\partial n(x,t)}{\partial x} = g(x,t) \tag{3}$$

where p and n are the densities of the holes and electrons, $g(x,t)$ is the volume generation rate, and v_p and v_n are the hole and electron velocities, respectively. We assume a saturated hole velocity of 4.8×10^6 cm/s and a saturated electron velocity of 6.5×10^6 cm/s for the intrinsic layer [10]. At the resonant condition, the light intensity distribution within the i region can be expressed as a function of $\sin^2(a_1 x + a_2)$ (see Fig. 4). In the present calculations, $a_1 = 2\pi/4L_i$, and $a_2 = 0 \sim \pi/2 (a_2 = \pi/2$ for Profile 1 and $a_2 = 0$ for Profile 2). Consider a sinusoidal modulation of optical power illuminate upon the RCE photodiode, the time variation of the generation rate can be expressed in the following form:

$$g(x,t) = g_0 \sin^2(a_1 x + a_2)(1 + m \exp(i\omega t)) \tag{4}$$

where m is a modulation index and g_0 is a normalization constant. Substituting (4) into (3) together with the boundary conditions $p(L_i) = 0$ and $n(0) = 0$, we get

$$p(x,t) = B_p(x) + D_p(x,\omega)\exp(i\omega t) \tag{5a}$$
$$n(x,t) = B_n(x) + D_n(x,\omega)\exp(i\omega t) \tag{5b}$$

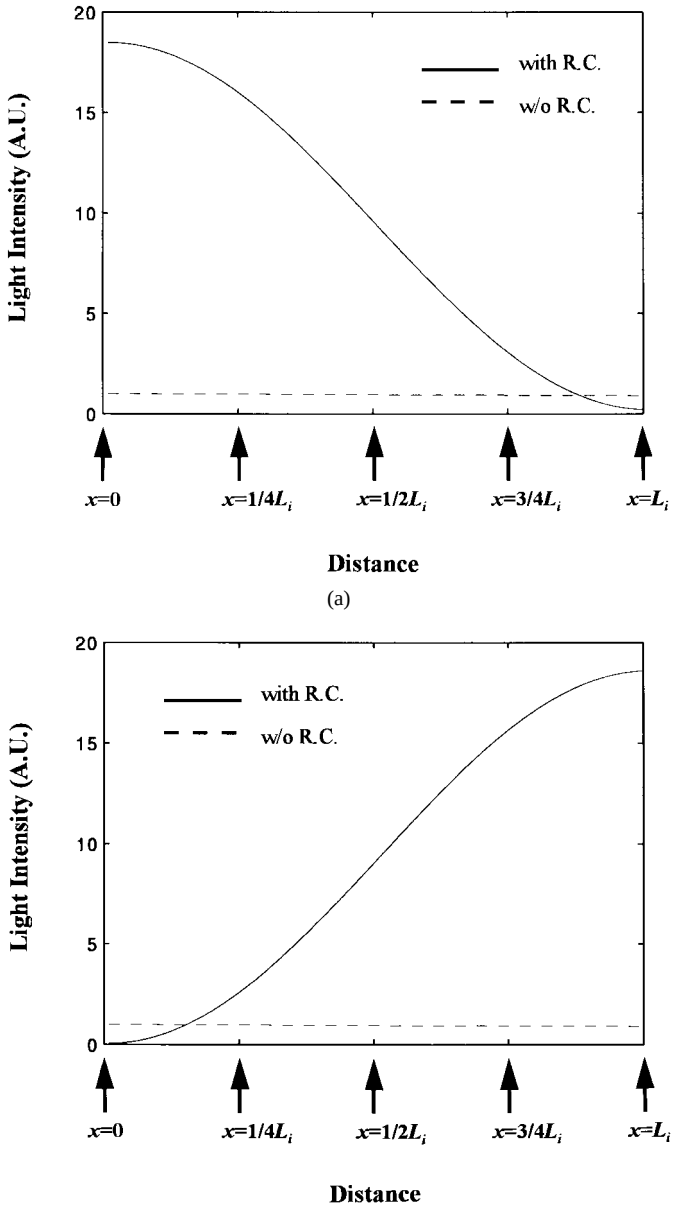

Fig. 4. Light field distribution within the i region of the studied RCE photodiode as a function of position for (a) $L_p = \lambda, L_n = \lambda$ and (b) $L_p = 3/4\lambda, L_n = 5/4\lambda$. The dashed curve is for the conventional photodiode without resonant cavity.

where

$$B_p(x) = \frac{g_0}{4a_1 v_p}\{2a_1(x - L_i) + \sin(2a_2) - \sin[2\alpha_1(x - L_i) + 2a_2]\} \tag{6a}$$
$$B_n(x) = -\frac{g_0}{4a_1 v_n}\{2a_1 x + \sin(2\alpha_2) - \sin[2a_1 x + 2a_2]\} \tag{6b}$$
$$D_p(x,\omega) = A_1[A_2 + A_3 + A_4 \cos(2a_1 x + 2a_2) + A_5 \sin(2a_1 x + 2a_2)] + C_1 \exp(-i\omega\tau_p) \tag{6c}$$
$$D_n(x,\omega) = A_6[A_7 + A_8 + A_9 \cos(2a_2 x + 2a_2) + A_{10} \sin(2a_1 x + 2a_2)] + C_2 \exp(i\omega\tau_n). \tag{6d}$$

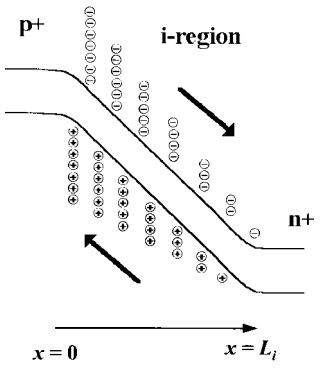

(a)

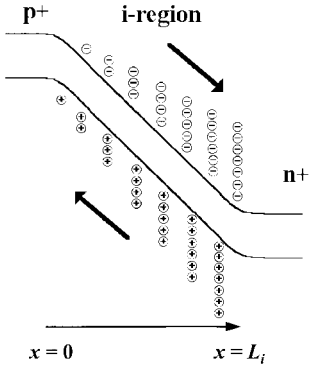

(b)

Fig. 5. Photocarrier distribution profiles for different combinations of L_p and L_n. (a) When $L_p = \lambda, L_n = \lambda$, the maximum occurs at the p^+ edge of the i region. (b) When $L_p = 3/4\lambda, L_n = 5/4\lambda$, the maximum occurs at the n^+ edge of the i region.

$\tau_p\ (= L_i/v_p)$ and $\tau_n (= L_i/v_n)$ are the electron and the hole transit times, respectively, $A_1 \sim A_{10}$ and C_1, C_2 are given in Appendix A. The current density in the diode is

$$\begin{aligned} J(\omega) &= \frac{q}{L_i}\int_0^{L_i}[v_p p(x,t) + v_n n(x,t)]\,dx \\ &= \frac{q}{L_i}\int_0^{L_i}[v_p B_p(x) + v_n B_n(x)]\,dx \\ &\quad + \frac{q}{L_i}\int_0^{L_i}[v_p D_p(x,\omega) + v_n D_n(x,\omega)]\exp(i\omega t)\,dx \\ &= J_0 + J_s(\omega)\exp(i\omega t) \end{aligned} \tag{7}$$

where q is the electronic charge, J_0 is the DC component, $J_s(\omega)$ is the signal current density, and

$$J_s(\omega) = J_p(\omega) + J_n(\omega) \tag{8}$$

where

$$\begin{aligned} J_p(\omega) = \frac{qA_1}{\tau_p}\Bigg\{ & L_i(A_2 + A_3) + \frac{A_4}{2a_1}[-\sin(2a_2) \\ & + \sin(2a_1 L_i + 2a_2)] + \frac{A_5}{2a_1}[\cos(2a_2) \\ & - \cos(2a_1 L_i + 2a_2]\Bigg\} + iC_1\frac{qv_p\tau_p}{\omega} \\ & \cdot[-1 + \exp(-i\omega\tau_p] \end{aligned} \tag{8a}$$

$$\begin{aligned} J_n(\omega) = \frac{qA_6}{\tau_n}\Bigg\{ & L_i(A_7 + A_8) + \frac{A_9}{2a_1}[-\sin(2a_2) \\ & + \sin(2a_1 L_i + 2a_2)] + \frac{A_{10}}{2a_1}[\cos(2a_2) \\ & - \cos(2a_1 L_i + 2a_2]\Bigg\} + iC_2\frac{qv_n\tau_n}{\omega} \\ & \cdot[1 - \exp(i\omega\tau_n)]. \end{aligned} \tag{8b}$$

The frequency response $F(\omega, v_p, v_n, a_1, a_2)$ is given by

$$F(\omega, v_p, v_n, a_q, a_2) = 20\log\left|\frac{J_s(\omega)}{J_s(0)}\right|. \tag{9a}$$

If the RC effect is included, then

$$F(\omega, v_p, v_n, a_1, a_2) = 20\log\left\{\frac{\left|\frac{J_s(\omega)}{J_s(0)}\right|}{\sqrt{1+\omega^2R^2C^2}}\right\}\ \text{(dB)} \tag{9b}$$

where R is the sum of the load resistance (R_L) and the diode series resistance (R_S) and C is the diode capacitance plus other parasitic capacitances. In this calculations, R is assumed to be 50 Ω and the diode area is assumed to be $2\,\mu\text{m} \times 2\,\mu\text{m}$. A reasonable value of C is taken to be 10 fF. Fig. 6 plots the frequency response calculated from (9b). If the light field distribution is Profile 2 [Fig. 4(a)], the calculated 3-dB frequency is 204 GHz. For Profile 1 [Fig. 4(b)], the calculated 3-dB frequency is about 234 GHz, and an increase of 30 GHz is observed. In Profile 1, most of the electron-hole pairs are generated near the p^+ edge of the depletion layer. The holes are collected immediately by the p^+ layer while the electrons drift through the depletion layer for a time $\tau_n\ (= L_i/v_n)$, which depends on the electron saturation drift velocity v_n. If most of the carriers were generated near the n^+ edge of the depletion layer (Profile 2), the transit time and the current would be determined by the hole saturation drift velocity v_p. Since v_n $(= 6.5 \times 10^6$ cm/s) is greater than v_p $(= 4.8 \times 10^6$ cm/s), a bandwidth increase for Profile 1 is expected. If the ratio of v_n/v_p is larger, the difference will be even more evident. The frequency response of the photodiode without a resonant cavity is also shown in Fig. 6 (the dashed–dotted curve) for comparison. The calculated 3-dB frequency is about 216 GHz (Appendix B). For such devices, there is no enhancement for the optical field due to resonance and the light is absorbed almost uniformly in the i region because the i layer is very thin (less than 0.1 μm); photocarriers are generated everywhere in the depletion region.

Fig. 7 shows the 3-dB frequency (or bandwidth) as a function of the L_p/L_n ratio. $L_p + L_n$ was kept at 2λ to ensure the resonant condition. From Figs. 3 and 7, we obtain the gain–bandwidth product which is shown in Fig. 8. We can see that $L_p = \lambda, L_n = \lambda$ (or thicknesses differ by $1/2\lambda$) gives the best gain-bandwidth product and is the optimum design for the present structure. To emphasize further the influence of optical field distribution on the speed of a RCE photodiode, the

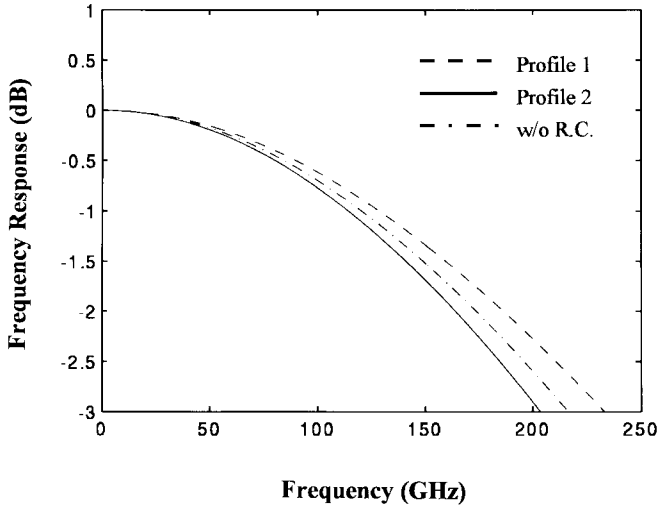

Fig. 6. Calculated frequency response of the studied RCE photodiode. The dashed line shows the response with Profile 1 and the solid line shows the response with Profile 2. Also shown is the calculated response for the conventional photodiode without resonant cavity (dashed–dotted line).

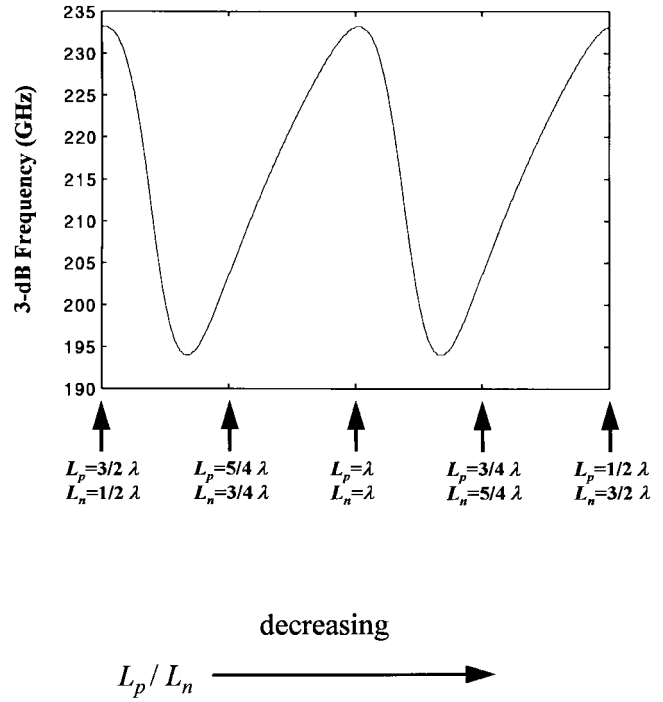

Fig. 7. Thickness dependence of the 3-dB frequency (or bandwidth) for various combinations of L_p and L_n. To operate the RCE photodiode at the resonant condition, $L_p + L_n$ is kept as a constant of 2λ.

response of the photodiode to an impulse of light is computed in the next section.

IV. Impulse Response and Step Response

A. Impulse Response

Consider a situation in which an impulse of optical power generates N electron-hole pairs at $t = 0$ according to the light field distribution. As described earlier, the carrier density

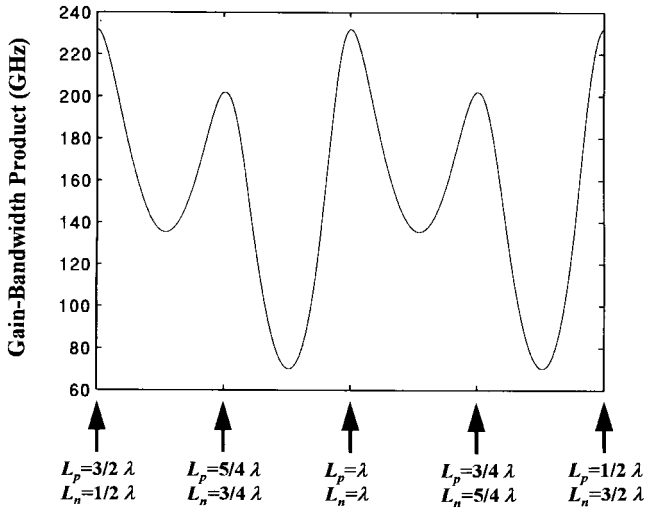

Fig. 8. Thickness dependence of the gain-bandwidth product for various combinations of L_p and L_n. The maximum is about 231 GHz at $L_p = \lambda, L_n = \lambda$ (Profile 1).

distribution function $n(x)$ can be expressed as

$$n(x) = N_0 \sin^2(a_1 x + a_2) \tag{10}$$

where N_0 is a normalization factor and

$$\begin{aligned} N &= \int_0^{L_i} n(x)\,dx \\ &= \int_0^{L_i} N_0[\sin^2(a_1 x + a_2)]\,dx \end{aligned}$$

from which we get

$$N_0 = \frac{4a_1 N}{\sin(2a_2) + 2a_1 L_i - \sin(2a_1 L_i + 2a_2)}. \tag{11}$$

After a period of time t, part of the carriers drift out of the depletion region, and the average electron density left within the i layer becomes

$$\begin{aligned} n(t) &= \frac{1}{L_i}\left\{\int_0^{L_i} N_0 \sin^2[a_1(x - v_n t) + a_2]\,dx\right\} \\ &\quad \cdot \mathrm{U}(\tau_n - t), \qquad t \geq 0 \\ &= \frac{N_0}{L_i}\left\{\frac{1}{2}(L_i - v_n t) + \frac{1}{4a_1}[\sin(2a_2) \right. \\ &\quad \left. - \sin(2a_1(L_1 - v_n t) + 2a_2)]\right\} \mathrm{U}(\tau_n - t), \\ &\quad t \geq 0 \end{aligned}$$

where U is the unit step function. The electron current density is

$$\begin{aligned} J_n(t) &= qn(t)v_n \\ &= \frac{qN_0}{4a_1\tau_n}\{2a_1(L_i - v_n t) + \sin(2a_2) \\ &\qquad - \sin[2a_1(L_i - v_n t) + 2a_2]\} \\ &\qquad \cdot \mathrm{U}(\tau_n - t), \qquad t \geq 0. \end{aligned} \tag{12a}$$

Similarly, the number of holes inside the i layer at time t is

$$\begin{aligned} p(t) &= \frac{1}{L_i}\left\{\int_0^{L-i-v_p t} N_0 \sin^2[a_1(x + v_p t) + a_2]\,dx\right\} \\ &\qquad \cdot \mathrm{U}(\tau_p - t), \qquad t \geq 0 \\ &= \frac{N_0}{L_i}\left\{\frac{1}{2}(L_i - v_p t) + \frac{1}{4a_1}[\sin(2a_1 v_p t + 2a_2) \right. \\ &\qquad \left. - \sin(2a_1 L_i + 2a_2)]\right\}\mathrm{U}(\tau_p - t), \quad t \geq 0 \end{aligned}$$

and the hole current density is

$$\begin{aligned} J_p(t) &= qp(t)v_p \\ &= \frac{qN_0}{4a_1\tau_p}\{2a_1(L_i - v_p t) + \sin(2a_1 v_p t + 2a_2) \\ &\qquad - \sin(2a_1 L_i + 2a_2)\}\mathrm{U}(\tau_p - t), \quad t \geq 0. \end{aligned} \tag{12b}$$

The total current density is then

$$J_{\mathrm{imp}}(t) = J_n(t) + J_p(t). \tag{13}$$

Fig. 9 shows the calculated current impulse response. An important figure of merit for digital circuit applications is the fall time, t_f, which is defined as the time when the current density falls from 90% of the initial value to 10% of the initial value. The calculate t_f is 1.570 ps for Profile 2 and 1.086 ps for Profile 1. A 50% improvement in t_f is obtained. Since most of the holes in Profile 2 have to take a longer time to drift out of the i region, a clear "tail" is observed in Fig. 9, and that explains why Profile 2 has a much longer t_f. So, for the purpose of high-bit-rate communication, it is a better choice to use Profile 1 in the design of a RCE photodetector. Also shown in Fig. 9 is the impulse response for the photodiode without a resonant cavity; the calculated t_f is 1.289 ps (see Appendix C).

B. Step Response

Since the continuity equations in (3) are linear, the response to an arbitrary input function $X(t)$ is then found by convolving impulse response, J_{imp}, with $X(t)$ [14]:

$$J(t) = J_{\mathrm{imp}} * X(t) = \int_{-\infty}^{\infty} J_{\mathrm{imp}}(t')X(t - t')\,dt'. \tag{14}$$

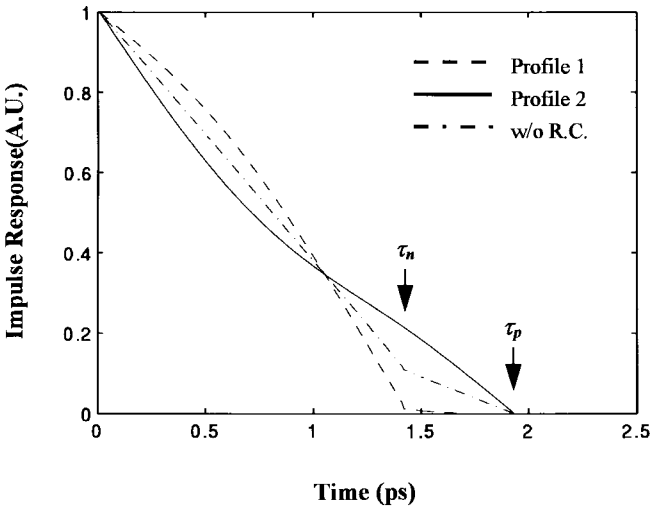

Fig. 9. Impulse response for the studied RCE photodiode. The dashed line shows the response with Profile 1 and the solid line shows the response with Profile 2. Also shown is the calculated response for the conventional photodiode without resonant cavity (dashed–dotted line).

For unit step response,

$$X(t) = \begin{cases} 0, & t < 0 \\ \mathrm{U}(t), & t > 0. \end{cases} \tag{15}$$

Substituting (13) and (15) into (14), we have

$$J_{\mathrm{step}}(t) = J_{n,\mathrm{step}}(t) + J_{p,\mathrm{step}}(t) \tag{16}$$

where

$$\begin{aligned} J_{n,\mathrm{step}}(t) &= \frac{qN_0}{8a_1^2 L_i}\{\cos(2a_1 L_i + 2a_2) + 4a_1^2 L_i v_n t \\ &\qquad - 2a_1^2 v_n^2 t^2 - \cos[2a_1(L_i - v_n t) + 2a_2] \\ &\qquad + 2a_1 v_n \sin(2a_2)t\}, \qquad 0 \leq t < \tau_n \\ &= \frac{qN_0}{8a_1^2 L_i}\{\cos(2a_1 L_i + 2a_2) + 2a_1^2 L_i^2 \\ &\qquad - \cos(2a_2) + 2a_1 L_i \sin(2a_2)\}, \qquad t \geq \tau_n. \end{aligned} \tag{17a}$$

$$\begin{aligned} J_{p,\mathrm{step}}(t) &= \frac{qN_0}{8a_1^2 L_i}\{\cos(2a_2) + 4a_1^2 L_i v_p t - 2a_1^2 v_p^2 t^2 \\ &\qquad - \cos(2a_1 v_p t + 2a_2) \\ &\qquad - 2a_1 v_p \sin(2a_1 L_i + 2a_2)t\}, \quad 0 \leq t < \tau_p \\ &= \frac{qN_0}{8a_1^2 L_i}\{\cos(2a_2) + 2a_1^2 L_i^2 - \cos(2a_1 L_i + 2a_2) \\ &\qquad - 2a_1 L_i \sin(2a_1 L_i + 2a_2)\}, \quad t \geq \tau_p. \end{aligned} \tag{17b}$$

The calculated step response of (16) is plotted in Fig. 10. If we define the rise time t_r as the time when J_{step} changes from 10% of the final value to 90% of the final value, the calculated t_r is 0.945 ps for Profile 1, 1.234 ps for Profile 2, and 1.078 ps for the conventional photodiode (see Appendix D), respectively. The influence of the light field distribution on the performance of step response is again very clear.

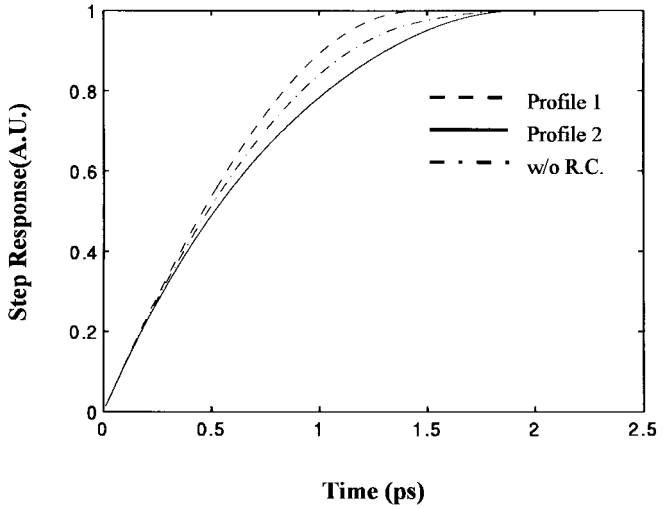

Fig. 10. Step response for the studied RCE photodiode. The dashed line shows the response with Profile 1 and the solid line shows the response with Profile 2. Also shown is the calculated response for the conventional photodiode without resonant cavity (dashed–dotted line).

V. Conclusion

We have studied the high-speed performance of a double-heterostructure RCE p-i-n photodiode. At the resonant condition, by varying the length of L_p (L_n) while keeping $L_p + L_n$ constant, we can obtain different light field distributions. By properly choosing L_p (L_n), we can obtain an optimum structure where the maximum light intensity occurs near the p^+ edge of the i layer. In such a structure, most of the generated holes are collected immediately by the p^+ layer while the electrons drift through the depletion layer with a larger drift velocity. By theoretically solving the linearized continuity equations, the calculated 3-dB frequency, gain-bandwidth product, impulse response, and step response all demonstrate the superiority of Profile 1 over Profile 2. So in a RCE structure, one can take advantage of the flexibility of cavity design to tailor the light field distribution in the absorption region to improve the device speed. This concept, demonstrated in a photodetector in this work, should also be useful for other optoelectronic devices.

Appendix A

The parameters used in (6) are

$$A_1 = \frac{ig_0 m}{2\omega(\omega^2 - 4a_1^2 v_p)}$$
$$A_2 = 4a_1^2 v_p^2$$
$$A_3 = -\omega^2$$
$$A_4 = \omega^2$$
$$A_5 = -2ia_1 v_p \omega$$
$$A_6 = \frac{ig_0 m}{2\omega(\omega^2 - 4a_1^2 v_n)}$$
$$A_7 = 4a_1^2 v_n^2$$
$$A_8 = A_3$$
$$A_9 = A_4$$
$$A_{10} = 2ia_1 v_p \omega$$
$$C_1 = -A_1[A_2 + A_3 + A_4 \cos(2a_1 L_i + 2a_2) + A_5 \sin[2a_1 L_i + 2a_2)] \exp(i\omega\tau_p)$$
$$C_2 = -A_6[A_7 + A_8 + A_9 \cos(2a_2) + A_{10} \sin(2a_2)].$$

Appendix B

The frequency response of a conventional p-i-n photodetector with light incident from the p side is (B1) [15], shown at the bottom of the page. For n-side illumination, (B1) is valid if the subscripts p and n are switched.

Appendix C

For a p-side illuminated p-i-n photodetector without a resonant cavity, we have

$$N = \int_0^{L_i} N_0 \exp(-\alpha x)\, dx = \frac{N_0}{\alpha}[1 - \exp(-\alpha L_i)]. \tag{C1}$$

From (C1), we get

$$N_0 = \frac{\alpha N}{1 - \exp(-\alpha L_i)}.$$

The average electron density within the i layer is

$$n(t) = \frac{1}{L_i}\left\{\int_{v_n t}^{L_i} N_0 \exp[-\alpha(x - v_n t)]\, dx\right\} \mathrm{U}(\tau_n - t) = \frac{N_0}{\alpha L_i}\{1 - \exp[-\alpha(L_i - v_n t)]\}\mathrm{U}(\tau_n - t)$$

and the electron current density is

$$J_n(t) = qn(t)v_n = \frac{qN_0}{\alpha\tau_n}\{1 - \exp[-\alpha(L_i - v_n t)]\}\mathrm{U}(\tau_n - t), \quad t \geq 0.$$

Similarly,

$$p(t) = \frac{1}{L_i}\left\{\int_0^{L_i - v_p t} N_0 \exp[-\alpha(x + v_n t)]\, dx\right\} \mathrm{U}(\tau_p - t) = \frac{N_0}{\alpha L_i}\{-\exp(-\alpha L_i) + \exp(-\alpha\nu_p t)\}\mathrm{U}(\tau_p - t)$$

$$\frac{J(\omega)}{J(0)} = \frac{1}{1 - \exp(-\alpha L_i)}\left[\frac{\exp(i\omega\tau_p - \alpha L_i) - 1}{i\omega\tau_p - \alpha L_i} - \exp(-\alpha L_i)\frac{\exp(i\omega\tau_p) - 1}{i\omega\tau_p} + \frac{\exp(i\omega\tau_n) - 1}{i\omega\tau_n} + \exp(-\alpha L_i)\frac{1 - \exp(\alpha L_i + i\omega\tau_n)}{\alpha L_i + i\omega\tau_n}\right] \tag{B1}$$

and the hole current density is

$$J_p(t) = qp(t)v_p = \frac{qN_0}{\alpha\tau_p}\{-\exp(-\alpha L_i) + \exp(-\alpha v_p pt)\}\mathrm{U}(\tau_p - t), \quad t \geq 0.$$

The total current density is

$$J_{\mathrm{imp}}(t) = J_n(t) + J_p(t). \tag{C2}$$

APPENDIX D

The step response for a conventional p-i-n photodetector with p-side illumination can be calculated directly by convolving the impulse response (C2) with unit step function $X(t)$. Substituting (C2), $X(t)$ into (14), we obtain

$$J_{\mathrm{step}}(t) = J_{n,\mathrm{step}}(t) + J_{p,\mathrm{step}}(t)$$

where

$$J_{n,\mathrm{step}}(t) = \frac{qN_0}{\alpha\tau_n}\left\{t + \frac{1}{\alpha v_n}\exp(-\alpha L_i)[1 - \exp(\alpha v_n t)]\right\}, \quad 0 \leq t < \tau_n$$

$$= \frac{qN_0}{\alpha\tau_n}\left\{\tau_n - \frac{1}{\alpha v_n}[1 - \exp(-\alpha L_i)]\right\}, \quad t \geq \tau_n$$

and

$$J_{p,\mathrm{step}}(t) = \frac{qN_0}{\alpha\tau_p}\left\{-t\exp(-\alpha L_i) + \frac{1}{\alpha v_p}[1 - \exp(\alpha v_p t)]\right\}, \quad 0 \leq t < \tau_p$$

$$= \frac{qN_0}{\alpha\tau_p}\left\{\frac{1}{\alpha v_p}\left(\tau_p - \frac{1}{\alpha v_p}\right)\exp(-\alpha L_i)\right\}, \quad t \geq \tau_p.$$

REFERENCES

[1] H. David Law, *Semiconductor and Semimetals, Lightwave Communication Technology*, Part D, vol. 22, p. 454, 1985.

[2] A. L. Gutierrez-Aitken, K. Yang, G. I. Haddad, P. Bhattacharya, and M. Lunardi, "16-Ghz bandwidth InAlAs-InGaAs monolithically integrated p-i-n/HBT photoreceiver," *IEEE Photon. Technol. Lett.*, vol. 7, pp. 1339–1341, 1995.

[3] K. Kishino, M. S. Unlu, J. I. Chyi, J. Reed, L. Arsenault, and H. Morkoc, "Resonant cavity-enhanced (RCE) photodetectors," *IEEE J. Quantum Electron.*, vol. 27, pp. 2025–2034, 1991.

[4] A. Salvador, F. Huang, B. Sverdlov, A. E. Botchkarev, and H. Morkoc, "InP/InGaAs resonant cavity enhanced photodetector and light emitting diode with external mirrors on Si," *Electron. Lett.*, vol. 30, pp. 1527–1529, 1994.

[5] P. Guy, K. Woodbridge, S. K. Haywood, and M. Hopkinson, "Highly doped 1.55 μm $Ga_xIn_{1-x}As$/InP distributed Bragg reflector stacks," *Electron. Lett.*, vol. 30, pp. 1526–1527, 1994.

[6] C. C. Barron, C. J. Mahon, B. J. Thibeault, G. Wang, W. Jiang, L. A. Goldren, and J. E. Bowers, "Resonant-cavity-enhanced pin photodetector with 17 GHz bandwidth-efficiency product," *Electron. Lett.*, vol. 30, pp. 1796–1797, 1994.

[7] I. H. Tan, E. L. Hu, J. E. Bowers, and B. I. Miller, "Modeling and performance of wafer-fused resonant-cavity enhanced photodetectors," *IEEE Quantum Electron.*, vol. 31, pp. 1863–1875, 1995

[8] Y. G. Wey, D. L. Crawford, K. Giboney, J. E. Bowers, and M. J. Rodwell, "Ultrafast graded double-heterostructure GaInAs/InP photodiode," *Appl. Phys. Lett.*, vol. 58, pp. 2156–2158, 1991.

[9] Y. G. Wey, K. S. Giboney, J. E. Bowers, M. J. W. Rodwell, P. Silvestre, P. Thiagarajan, and G. Y. Robinson, "108 Ghz GaInAs/InP p-i-n photodiodes with integrated bias tees and matched resistors," *IEEE Photon. Technol. Lett.*, vol. 5, pp. 1310–1312, 1993.

[10] J. E. Bowers and C. A. Burrus, "Ultrawide-band long-wavelength p-i-n photodetectors," *J. Lightwave Technol.*, vol. LT-5, pp. 1339–1350, 1987.

[11] G. R. Fowles, *Introduction to Modern Optics*. New York: Holt, Rinehart and Winston, 1975, p. 100.

[12] M. S. Unlu, K. Kishino, H. J. Liaw, and H. Markoc, "A theoretical study of resonant cavity-enhanced photodetectors with Ge and Si active regions," *J. Appl. Phys.*, vol. 71, pp. 4049–4058, 1992.

[13] G. Lucovsky, R. F. Schwarz, and R. B. Emmons, "Transit-time considerations in p-i-n diodes," *J. Appl. Phys.*, vol. 35, pp. 622–628, 1964.

[14] A. B. Carlson, *Communication Systems*, 2nd ed. New York: McGraw-Hill, 1975.

[15] J. E. Bowers, C. A. Burrus, and R. J. Mccoy, "InGaAs pin photodetectors with modulation response to millimeter wavelengths," *Electron. Lett.*, vol. 21, pp. 812–814, 1985.

Hsin-Han Tung, photograph and biography not available at the time of publication.

Chien-Ping Lee (M'80–SM'94), photograph and biography not available at the time of publication.